

# Search for the rare fully leptonic decay

$$B^+ \rightarrow \mu^+ \mu^- \mu^+ \nu \text{ at LHCb}$$

Slavomira Stefkova

High Energy Physics

Blackett Laboratory

Imperial College London

A thesis submitted to Imperial College London  
for the degree of Doctor of Philosophy

# Abstract

This thesis reports the branching fraction measurement of the rare Cabibbo-suppressed decay  $\Lambda_b^0 \rightarrow p\pi^-\mu^+\mu^-$ . The decay is observed for the first time with a  $5.5\sigma$  deviation from the background-only hypothesis. This is the first observation of a  $b \rightarrow d$  quark transition in the baryon sector. The dataset used for the measurement corresponds to  $3 \text{ fb}^{-1}$  of  $pp$  collisions collected at the LHCb experiment at CERN. The branching fraction is measured using  $\Lambda_b^0 \rightarrow J/\psi (\rightarrow \mu^+\mu^-)p\pi^-$  as a normalisation channel and is measured as

$$\mathcal{B}(\Lambda_b^0 \rightarrow p\pi^-\mu^+\mu^-) = (6.9 \pm 1.9 \pm 1.1_{-1.0}^{+1.3}) \times 10^{-8},$$

where the first error is the statistical uncertainty, the second is the systematic uncertainty and the third is the uncertainty on  $\mathcal{B}(\Lambda_b^0 \rightarrow J/\psi p\pi^-)$ . The measurement of  $\mathcal{B}(\Lambda_b^0 \rightarrow p\pi^-\mu^+\mu^-)$  can be combined with the branching fraction measurement for  $\Lambda_b^0 \rightarrow pK^-\mu^+\mu^-$  to give constraints on the ratio of CKM matrix elements  $|\frac{V_{td}}{V_{ts}}|$ . Such a determination of  $|\frac{V_{td}}{V_{ts}}|$  requires a theory prediction for the ratio of the relevant form factors.

This thesis also reports the ratio of tracking efficiencies,  $\epsilon_{\text{rel}}$ , between data and simulation for  $K_s^0 \rightarrow \pi^+\pi^-$  decays occurring within the LHCb detector acceptance. As  $K_s^0$  particles are long-lived, their associated tracking efficiencies are less precisely determined compared to those of shorter-lived particles. The average value of  $\epsilon_{\text{rel}}$  for  $K_s^0 \rightarrow \pi^+\pi^-$  decays, where the  $K_s^0$  has a flight distance of  $\gtrsim 1 \text{ m}$ , is found to be

$$\epsilon_{\text{rel}} = 0.70 \pm 0.02.$$

To perform this calibration measurement a novel technique was developed which has the potential to be used in measuring the value of  $\epsilon_{\text{rel}}$  for other decays involving

long-lived particles.

# Contents

<b>Declaration of originality</b>	<b>5</b>
<b>Copyright declaration</b>	<b>6</b>
<b>Acknowledgements</b>	<b>7</b>
<b>List of Figures</b>	<b>9</b>
<b>List of Tables</b>	<b>13</b>
<b>List of abbreviations and definitions</b>	<b>14</b>
<b>1 Introduction</b>	<b>17</b>
<b>2 The LHCb detector</b>	<b>18</b>
2.1 LHCb Layout . . . . .	19
2.2 VERtex LOCator . . . . .	23
2.3 Tracking System . . . . .	25
2.3.1 Tracking Algorithms . . . . .	26
2.4 Ring Imaging Detectors . . . . .	28
2.5 RICH Reconstruction and Performance . . . . .	30
2.5.1 RICH performance . . . . .	30
2.6 Calorimetry . . . . .	32
2.7 Muon Stations . . . . .	33

2.7.1	Muon Identification . . . . .	35
2.7.2	Muon Performance . . . . .	36
2.8	Trigger . . . . .	37
2.9	Simulation . . . . .	41
2.9.1	Differences in Simulation And Data . . . . .	42
<b>3</b>	<b>Discovering (Setting Limit for) <math>B^+ \rightarrow \mu^+ \mu^- \mu^+ \nu</math> at LHCb</b>	<b>44</b>
3.1	Topology of at LHCb $B^+ \rightarrow \mu^+ \mu^- \mu^+ \nu$ at LHCb . . . . .	44
3.2	Sources of Backgrounds . . . . .	47
	<b>Bibliography</b>	<b>48</b>
	<b>Appendices</b>	<b>52</b>
<b>A</b>	<b>Boosted Decision Trees</b>	<b>52</b>
<b>B</b>	<b>The <i>sPlot</i> technique</b>	<b>55</b>

# Declaration of originality

The work presented in this thesis is the result of collaborative work between members of the LHCb collaboration and myself. All the analysis work (chapters ??–??) presented in this thesis was performed by myself, with the exception of producing the simulation and data samples used in the analysis in ??. All work and plots presented in this thesis that were not the product of my own work are appropriately referenced.

This thesis has not been submitted for any other qualification.

Eluned Smith

September 2016

# Copyright Declaration

The copyright of this thesis rests with the author and is made available under a Creative Commons Attribution Non-Commercial No Derivatives licence. Researchers are free to copy, distribute or transmit the thesis on the condition that they attribute it, that they do not use it for commercial purposes and that they do not alter, transform or build upon it. For any reuse or redistribution, researchers must make clear to others the license terms of this work.

# Acknowledgements

Firstly, I would like to thank my supervisor Ulrik Egede. I would like to thank you for all the support, time and article corrections that you have invested in me. You have given me the opportunity to grow as physicist as well as you taught me to appreciate solving problems differently. You have given me the freedom to follow many different activities such as conferences, hardware, as well as detector maintenance all leading to meeting many great people that I am happy to call my friends.

To you Patrick Owen, I owe a big thank you for showing me all the support throughout my entire analysis. Without your great insight and motivation that you have kept even when you changed institute, it would have been completely different journey.

I would also like to express special thanks to Mike McCainn, whose patience knows no limits, but apparently LHC's is 15 minutes. I learnt how handle many power-cycling buttons as well as croquet. Here I would also like to extend my gratitude to many of the RICH collaborators such as Antonis, Silvia, Roberta whom I have met while working with the upgrade.

And ofcourse all the Imperial crew: Dave, Andrei, Mitesh, Paula, Eluned, Will, Fede, Sophie, Matt, Felix and Malte, who all have their part in this work.

None of this would be possible without the STFC, the financial body on behalf of British government, who financially supported my PhD and the LHCb collaboration as a whole.

Lastly but most importantly, I would like to thank my family. I have never heard from you that something cannot be done. You have taught me to be curious, to be independent, to be strong. We have sacrificed the most precious commodity, time spent



together, in order for me to follow my interests. And below is just one example it was all worth it.

# List of Figures

2.1	Accelerator complex at CERN. The image is taken from [1]. . . . .	19
2.2	Angular production and acceptance of LHCb's $b\bar{b}$ pair (in red) as well as General Purpose Detector (in yellow). LHCb covers region with highest production cross-section at 8 TeV. These plots were produced using PYTHIA8 [2] simulation. This plot was taken from [3] (left). Probability of interaction per bunch crossing as a function of instantaneous luminosity. This figure was obtained from [4] (right). . . . .	20
2.3	The schematic slice of LHCb detector in $y, z$ plane where $z$ is defined to be the direction parallel to beamline, and $x, y$ define the plane perpendicular to the beamline. $\theta$ , the opening angle in $y-z$ plane with $\theta = 0$ along $z$ -axis. The figure was taken from [7]. . . . .	21
2.4	Integrated luminosity collected in different years of data-taking. This plot is taken from [8] (left). Development of the instantaneous luminosity for ATLAS, CMS and LHCb during LHC fill 2651. After ramping to the desired value of $4 \times 10^{32} cm^{-2}s^{-1}$ for LHCb, the luminosity is kept stable in a range of 5% for about 15 hours by adjusting the transversal beam overlap. The difference in luminosity towards the end of the fill between ATLAS, CMS and LHCb is due to the difference in the final focusing at the collision points, commonly referred to as the beta function, $\beta^*$ . This plot was obtained from [9] (right). . . . .	23

2.5	Schematic plot of <b>VELO</b> detector configuration along the beam pipe showing the layout as well as positions while in stable beams (discs have slight overlap) and injection. Figure taken from [10]. . . . .	24
2.6	Two key variables which quantify performance of the <b>VELO</b> detector. <b>IP</b> resolution which is worse for low momentum tracks (left) and <b>PV</b> resolution dependent on the number of tracks forming the primary vertex $N$ (right). Figures taken from [11]. . . . .	25
2.7	Visualisation of use of different technology with silicon technology in violet and straw-tube technology in cyan. The Figure was obtained in [12](left). Track types visualisation depending on which track stations provided hits. For the study of $B^+ \rightarrow \mu^+ \mu^- \mu^+ \nu$ decays only, <b>Long track</b> , are considered as muons will travel to the end of the detector leaving the hits all along. Figure is taken from [13] (right). . . . .	26
2.8	Momentum resolution of long tracks measured using "tag and probe" method at LHCb. The decay channel $J/\psi^+ \rightarrow \mu^+ \mu^-$ is analyzed. . . . .	28
2.9	Separation power for different species of particles in momentum-Cerenkov angle plane (left). Schematic diagram of RICH1 layout (right). Boths figures are taken from [10]. . . . .	29
2.10	Invariant mass distribution of $D^0$ data sample (in black) overlayed with fit to both background and signal (in blue) (left). An example of kaon <b>ID</b> (red) and <b>MisID</b> (black) efficiency as a funtion of momentum under two PID hypotheses, $DLL_K > 0$ (empty) and $DLL_K > 5$ (filled) (right). Boths figures are taken from [16]. . . . .	31
2.11	$\pi^+ \pi^-$ invariant mass distributions obtained using kinematic constraints only (left) and also using PID constraints (right) in order to isolate $B^0 \rightarrow \pi^+ \pi^-$ peak. This figure is taken from [17]. . . . .	32
2.12	Granularity of <b>ECAL</b> (left) and <b>HCAL</b> (right) detectors. The figure was taken from [10]. . . . .	33

2.13	(a) Layout of the muon detector x-z plane and (b) x-y plane. This figure is taken from [18]. . . . .	34
2.14	(a) Probability of correctly identifying muons as a function of momentum $p$ in the bins of $p_T$ for $J/\psi \rightarrow \mu^+ \mu^-$ with IsMuon constraint. (c) Probability of incorrectly identifying pion (b) proton and (d) kaon as muon with IsMuon. This figure is taken from [19]. . . . .	37
2.15	<b>TOS</b> efficiency as a function of $p_T$ for muon-based decisions (left). <b>TOS</b> efficiency for different decays using L0 hadron trigger lines. This figure is taken from [18]. . . . .	38
2.16	<b>HLT1</b> efficiencies of the corresponding triggers using the same proxy as in Figure 2.15. This figure is taken from [20]. . . . .	39
2.17	Trigger scheme differences between Run I and Run II. Figures obtained from [21] . . . . .	41
2.18	<b>IP</b> resolution in x-direction comparing the data and simulation output for 2012 data-taking period (left). <b>IP</b> resolution in x-direction comparing the data and simulation output for 2011 data-taking period as a function of angle, $\phi$ (right). This figures are taken from [11]. . . . .	43
3.1	Schematic view of $B^+ \rightarrow \mu^+ \mu^- \mu^+ \nu$ decay. At $pp$ interaction point, or $PV$ , $b\bar{b}$ pair hadronizes into $B^\pm$ . $B^\pm$ flies some distance before decaying into three muons and neutrino. All charged tracks (in filled-blue) seen can be combined into four-vector representing the visible part of the decay (semifilled-blue). Information about invisible neutrino (semifilled-red) are deduced from the conservation of momentum with respect to the direction of the flight of $B^\pm$ . Neglecting momentum component parallel to the direction of flight for neutrino, transverse component of momentum is given. . . . .	45

A.1	An example decision tree. The S and B stand for ‘Signal-like’ and ‘Background-like’. The $\beta_i$ variables refer to the cut values chosen by the machine learning algorithm after the tree has been trained on signal and background samples. The blue ovals represent final nodes called leafs, which each leaf having an associated purity, i.e. the fraction of the weight of a leaf due to signal events. . . . .	53
-----	---	----

# List of Tables

2.1	Running conditions of LHC and LHCb in different years of data-taking. The statistics of LHCb’s instantenous luminosity is extracted using run database. . . . .	22
2.2	Momentum-dependent definition IsMuon variable. . . . .	36

# List of abbreviations and definitions

**ALICE** A Large Ion Collider Experiment.

**ATLAS** A Toroidal LHC ApparatuS.

**BDT** Boosted Decision Tree, a BDT employs multivariate analysis techniques to combine a set of weakly discriminating variables into a single discriminating variable.

**CMS** Compact Muon Solenoid.

**ECAL** Electromagnetic calorimeter.

**FD** Flight Distance, how far a particle flies before decaying.

**FOI** Field of Interest.

**HCAL** hadronic calorimeter.

**HLT** High Level Trigger. The HLT is the software trigger which is applied after the **L0** trigger.

**HLT1** First stage of high level trigger.

**HLT2** Second stage of high level trigger.

**HPD** Photomultiplier tubes that collect Cerenkov light.

**ID** Probability of correctly identifying particle, given PID requirement.

**IP** Impact Parameter. The IP is defined as the distance between a track and the **PV** at the track's closest point of approach.

**IT** Inner trackers, the inner section of the T stations.

**L0** Level-0 trigger. The L0 is the first trigger to be applied and uses hardware to make decisions on events.

**LHCb** The Large Hadron Collider beauty experiment.

**long track** Long track is track category which classifies tracks that have hits in the VELO and the T stations. Hits in the TT stations are optional.

**LS1** Long Shutdown 1.

**M1-5** The five muon stations.

**MC** Monte Carlo Simulation.

**misID** Probability of incorrectly identifying particle given PID requirement.

**MWPCs** multi-wire proportional chambers.

**OT** Outer trackers, the outer section of the T stations.

**PID** Particle IDentification.

**PRS** pre-shower.

**PV** Primary Vertex, the  $pp$  interaction vertex.

**QED** Quantum Electrodynamics.

**RICH** Ring Imaging Cherenkov detectors, provide particle identification by using Cherenkov radiation.



**SM** Standard Model.

**SPD** Scintillator Pad Detectors.

**SV** Secondary Vertex.

**T1, T2 and T3** Trackers downstream of the magnet composed of silicon micro-strips strips in the inner section and straw tubes in the outer section..

**TIS** Events which are Triggered Independent of Signal.

**TISTOS** Events which require both the presence of signal and the rest of the event to fire the trigger.

**TOS** Events which are Triggered On Signal.

**TT** The tracking station upstream of the magnet composed of silicon micro-strips..

**VELO** VERtex LOcator. Subdetector of LHCb, placed around the  $pp$  interaction point, used to realise the precise measurements of vertices and tracks.

# Chapter 1

## Introduction

The Standard Model (**SM**) is an effective theory which describes fundamental particles and their interactions to an impressive precision.

bla

# Chapter 2

## The LHCb detector

In this section, overview of accelerator complex at CERN as well as physics motivation behind **LHCb** detector and its details will be described.

CERN built one of the most exciting laboratories to study elementary particle interactions. The complex set of particle accelerators and detectors is shown in [Figure 2.1](#). The process of accelerating protons starts with the source of protons. Protons are obtained from hydrogen gas bottle by applying and an electric field separates hydrogen into positively and negatively charged constituents. The first proton accelerator in the chain, Linac 2, accelerates the protons to the energy of 50 MeV. It is a tank composed of several chambers where the resonant cavity is tuned to a specific frequency which creates potential differences in the cavities making accelerate the protons. These are then injected into the Proton Synchrotron Booster (PSB). Here the protons are accelerated to 1.4 GeV. The next line is the Proton Synchrotron (PS) reaching energy of 25 GeV. Before either entering the LHC or North Area (mainly used as testing facility for experiment upgrades) Super Proton Synchrotron (SPS) is the last stop. Here proton acceleration to 450 GeV is achieved.

The Large Hadron Collider (LHC) is a complex machine which accelerates beams of protons in opposite directions in

~

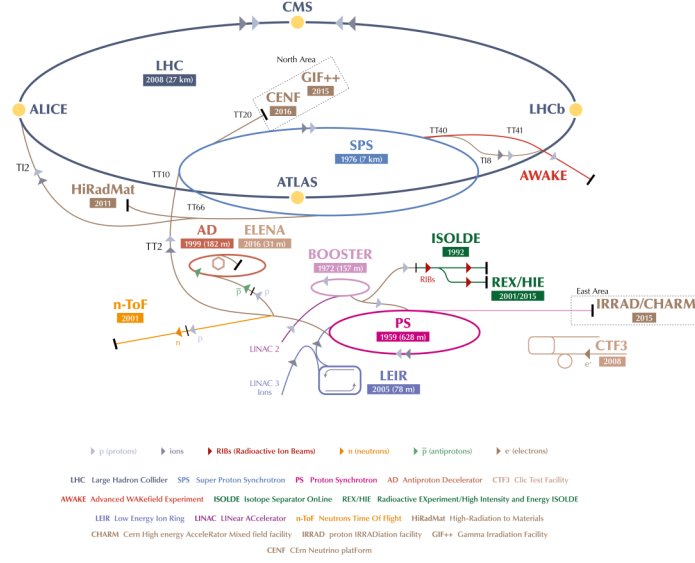


Figure 2.1: Accelerator complex at CERN. The image is taken from [1].

27km circular tunnel. It is located 50-157 m below ground on the border of Switzerland and France. Once the desired energy is achieved proton-proton,  $pp$ , or ion, collisions happen at four distinct points, where different detectors with different physics focus are located. These are **ATLAS**, **CMS**, **ALICE** and **LHCb**. Study of  $B^+ \rightarrow \mu^+ \mu^- \mu^+ \nu$  was performed using data obtained at **LHCb**.

## 2.1 LHCb Layout

**LHCb** differs from the other general purpose detectors on the LHC ring as its studies properties of heavy particles containing  $b$  or  $c$  quarks. This can be attributed to the geometrical acceptance and unique vertex resolution as well as excellent **PID**.

Contrary to the two general purpose detectors where the collisions are occurring in the centre of the detector, **LHCb**'s collision point is located at one end of the detector, hence its description as a forward single-arm spectrometer. This means that information about products outside of its scope are not known, meaning that there is no overall

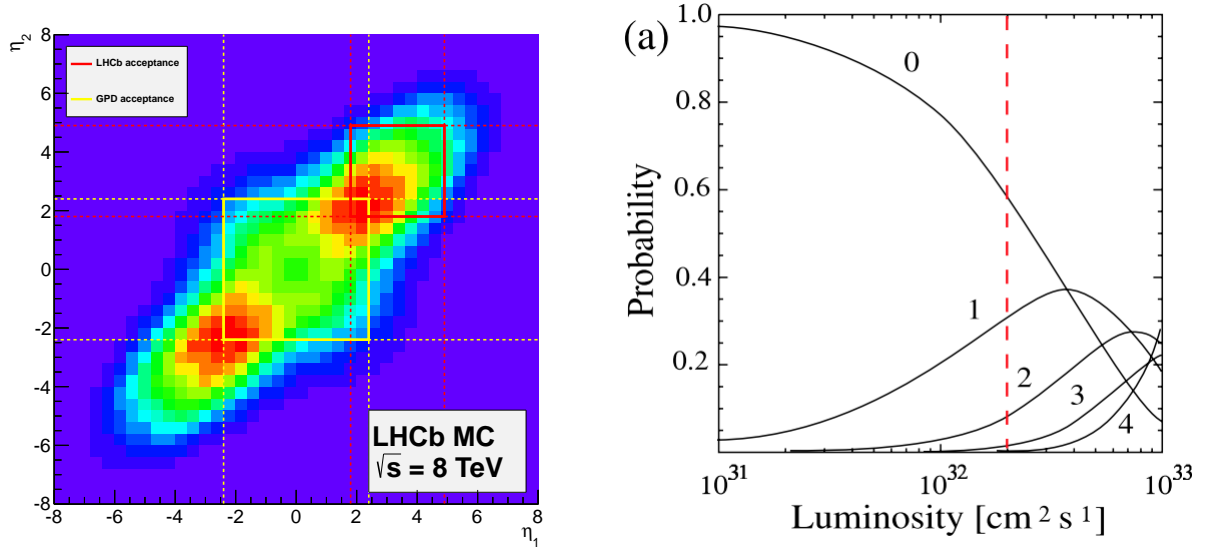


Figure 2.2: Angular production and acceptance of LHCb's  $b\bar{b}$  pair (in red) as well as General Purpose Detector (in yellow). **LHCb** covers region with highest production cross-section at 8 TeV. These plots were produced using PYTHIA8 [2] simulation. This plot was taken from [3] (left). Probability of interaction per bunch crossing as a function of instantaneous luminosity. This figure was obtained from [4] (right).

constraint on collision information, unlike in other flavour experiments. This is compensated by production mechanism of  $b\bar{b}$  and  $c\bar{c}$  in  $pp$  interactions, which occurs via gluon-gluon fusion. In this process, each gluon will carry part of proton's momentum. If the two gluons from two protons carry significantly different momentum, the  $b\bar{b}$  system will be boosted with respect to the  $pp$  rest frame, either in forward or backward cone closely to the beamline, as can be seen in Figure 2.2.

The angular coverage of **LHCb** is formally defined using pseudorapidity  $\eta$ ,

$$\eta = -\ln\left(\tan\frac{\theta}{2}\right) \quad (2.1)$$

where  $\theta$  is defined in Figure 2.3. **LHCb** detector, hence, covers the region  $2 < \eta < 5$ . The production cross-section of the fundamental process of  $pp \rightarrow b\bar{b}X$  was measured in this region yielding,  $\sigma(pp \rightarrow b\bar{b}X) = 75.3 \pm 5.4 \pm 13.0 \text{ } \mu\text{bb}$  at 7 TeV [5] and  $144 \pm 1 \pm 21 \text{ } \mu\text{b}$  at 13

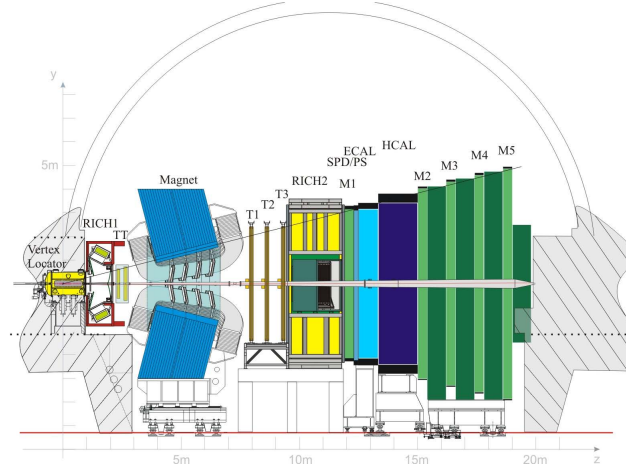


Figure 2.3: The schematic slice of **LHCb** detector in  $y, z$  plane where  $z$  is defined to be the direction parallel to beamline, and  $x, y$  define the plane perpendicular to the beamline.  $\theta$ , the opening angle in  $y-z$  plane with  $\theta = 0$  along  $z$  – axis. The figure was taken from [7].

TeV [6], which shows that the production cross-sections scales roughly linearly with the centre-of-mass energy. Assuming design conditions of LHCb, seen in Table 2.1,  $2 \text{ fb}^{-1}$  of data would correspond to  $10^{12}$  of  $b\bar{b}$  pairs being produced.

Despite such impressive statistics of  $b\bar{b}$  pairs available to **LHCb**, the bottleneck arises in much more copious inelastic background. It mostly originates from soft QCD processes which are related to the amount of pile-up, the visible number of  $pp$  interaction in the visible events. By looking at the probability of number of  $pp$  interaction per bunch crossing as a function of luminosity, shown in Figure 2.2, it can be noted that the maximum probability for only one  $pp$  interaction (and hence minimizing the background) is found to be at  $\sim 2 \times 10^{32} \text{ cm}^{-2} \text{ s}^{-1}$ , hence the LHCb design luminosity. In addition, to keep the occupancy of the detector reasonable, global event cuts, *GECs*, are put in the place, where only events with 600 (in 7,8 TeV) and 450 (in 13 TeV) tracks and less are allowed to be processed.

As **LHCb** requires much lower luminosity compared to other LHC detectors, it is achieved by LHCb-specific control of luminosity known as *luminosity levelling*. This

procedure achieves stable instantaneous luminosity by controlling that the two beams do not collide straight head-on at collision point, but are moved with respect to each other. It limits the effects of luminosity decay, which can lead to trigger alterations during specific data taking run, resulting in systematic uncertainties.

So far, the detector has been running since 2010, with collected integrated luminosity shown in Figure 2.4. As compared to ATLAS and CMS the integrated luminosity is much lower, due to allowed pile-up conditions. In 2017, there were two  $pp$  collision energies at which the data was taken: at  $\sqrt{s} = 13$  and 5 TeV. Run I data-taking (2010-2012) was paused by Long Shutdown 1 (LS1) and followed with Run II data-taking (2015-2018). The summary of LHCb running conditions is provided in Table 2.1, showing the evolution of the instantaneous luminosity as well as the frequency of collisions compared to the design proposal.

year	$\sqrt{s}$ [TeV]	Instantaneous Luminosity $\mathcal{L}$ [ $\times 10^{32} cm^{-2} s^{-1}$ ]
Design	Up to 14	2
2011	7	$\sim 3.0-3.5$
2012	8	$\sim 4.0$
2015	13	$\sim 0.5-4.5$
2016	13	$\sim 4.0$
2017	13	$\sim 4.0-6.0$

Table 2.1: Running conditions of LHC and LHCb in different years of data-taking. The statistics of LHCb's instantaneous luminosity is extracted using run database.

In the following sections, brief discussion of different subdetectors is presented. Both hardware and software overview will be presented with particular emphasis given to Muon Station and Simulation of LHCb.

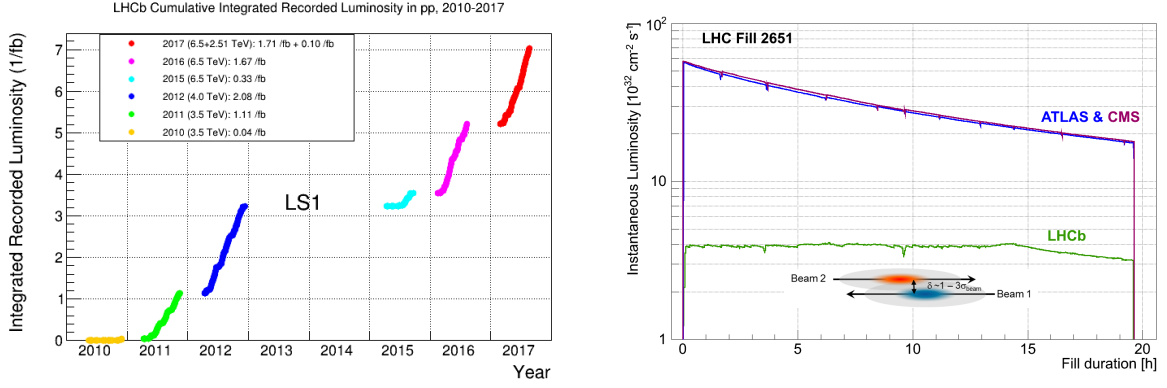


Figure 2.4: Integrated luminosity collected in different years of data-taking. This plot is taken from [8] (left). Development of the instantaneous luminosity for **ATLAS**, **CMS** and **LHCb** during LHC fill 2651. After ramping to the desired value of  $4 \times 10^{32} \text{ cm}^{-2} \text{ s}^{-1}$  for LHCb, the luminosity is kept stable in a range of 5% for about 15 hours by adjusting the transversal beam overlap. The difference in luminosity towards the end of the fill between ATLAS, **CMS** and **LHCb** is due to the difference in the final focusing at the collision points, commonly referred to as the beta function,  $\beta^*$ . This plot was obtained from [9] (right).

## 2.2 VErteX LOcator

The closest detector around the collision point is VErteX LOcator (**VELO**). This silicon-strip based detector, that extends 1 m along the beam axis, is primarily used for to distinguish events from prompt background. The typical differing property of a  $B$  hadron decay includes large impact parameter (**IP**), the minimal distance between the track and primary vertex, in addition to significantly higher transverse momentum  $p_T$ . Main uses of this subdetector include finding:

- primary vertices positions
- secondary vertices of short-lived particles (heavy quark hadrons)
- tracks that did NOT originate from primary vertex



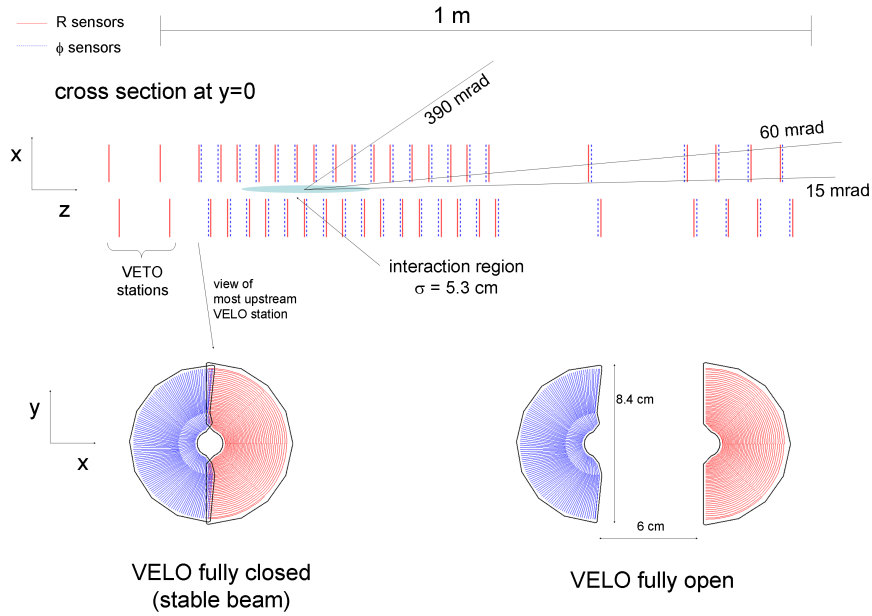


Figure 2.5: Schematic plot of **VELO** detector configuration along the beam pipe showing the layout as well as positions while in stable beams (discs have slight overlap) and injection. Figure taken from [10].

The detector consists of two sets of 21 silicon modules positioned around the beam pipe, where each module has 2 types of half-moon-shaped discs as seen in Figure 2.5. In the first disc type the strips are arranged to provide radial information ( $R$ ), whereas the second type provides azimuthal ( $\phi$ ) information. As  $pp$  interaction point brings high radiation dose for this detector, the first sensitive strip starts only at a distance of 8 mm once stable beams are declared. Throughout the beam injection, when the beam radius may be larger, the two sets are moved away 3 cm perpendicularly from the interaction point. For the ( $R$ ) sensor, the individual module's strip pitch, distance between two strips, varies from  $38 \mu\text{m}$  to  $102 \mu\text{m}$  away from the beam pipe, so that the hit occupancy is roughly even. Each **VELO** half is kept within an alluminum welded box causing material overlap once stable beams are declared. These boxes then create their own vacuum which is different to the nominal LHC vacuum in order to protect

the detector from any electromagnetic interference with the beam.

This setup brings outstanding hit resolution (4-40  $\mu\text{m}$ ), which in turn allows for very high impact parameter resolution and very good primary vertex resolution, as seen in Figure 2.6. This is indispensable not only in order to perform the precise measurements of  $B$  and  $D$  lifetimes, but also to resolve oscillations caused by  $B_s^0 - \bar{B}_s^0$  mixing occurring at 3 trillion Hz rate.

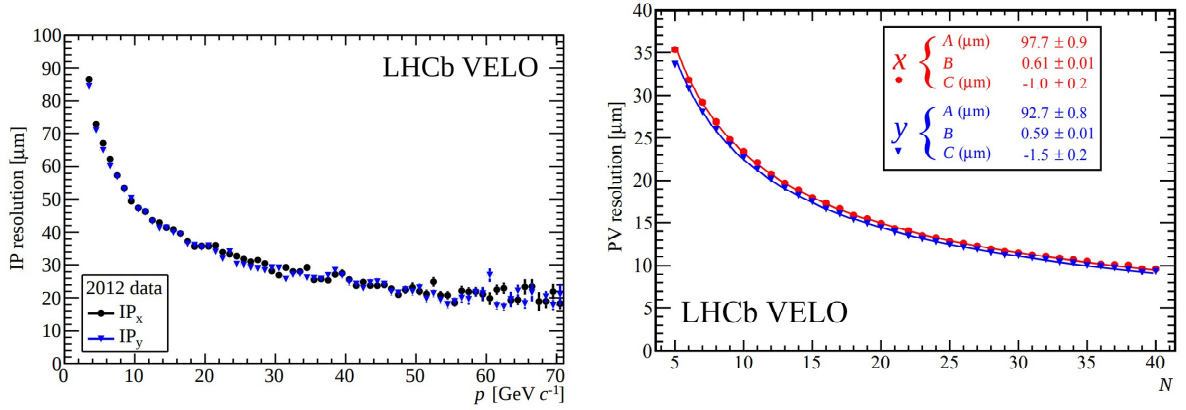


Figure 2.6: Two key variables which quantify performance of the **VELO** detector. **IP** resolution which is worse for low momentum tracks (left) and **PV** resolution dependent on the number of tracks forming the primary vertex  $N$  (right). Figures taken from [11].

## 2.3 Tracking System

In addition to tracking information provided by **VELO**, the trajectories of charged particles are monitored by series of tracking subdetectors. The main task of these tracking subdetectors is to provide efficient reconstruction and precise measurement of particle's momentum. There are four tracking stations apart from **VELO**: Tracker Turicensis (**TT**), positioned upstream from magnet, and **T1**, **T2** and **T3** tracking stations on the other side from the magnet. The 10 m dipole magnet with  $\approx 4$  Tm integrated field provides enough strength to bend charged particles with  $p$  of 200  $\text{GeV}/c^2$ .

Two different detection technologies are used in these trackers reflecting the nature

of track occupancy as function of distance from beam pipe. The tracker's part close to the beam pipe, **TT** station together with central region of T1-T3, also known as Inner Tracker (**IT**), expects higher occupancy and makes use of the silicon microstrip detection mechanism. The outer part of **T1**, **T2** and **T3** stations, also known as Outer Tracker **OT**, is made of straw-tube detectors. It measures the hit position by measuring the drift-time of ionized electrons. This two technologies are seen in Figure 2.7.

### 2.3.1 Tracking Algorithms

Different particles will leave different footprint in the detector. Charged particles will form tracks. Depending on presence of hits in individual subdetectors, they are grouped into several categories, visualized in Figure 2.7.

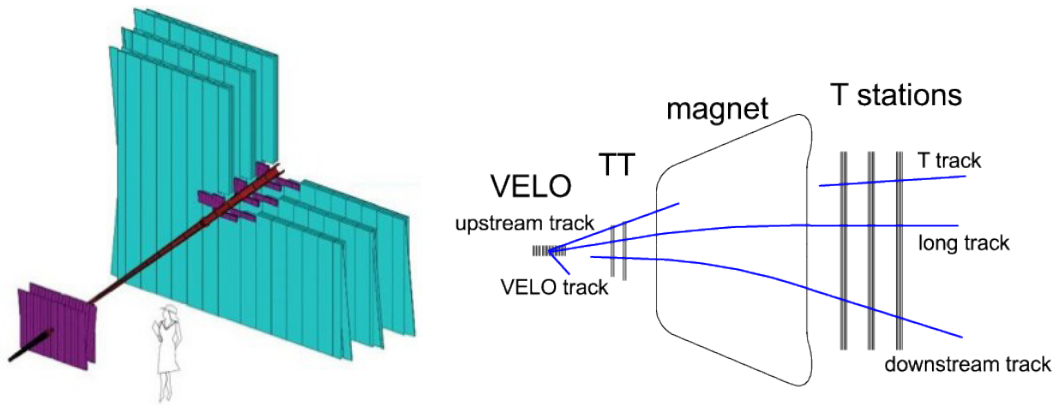


Figure 2.7: Visualisation of use of different technology with silicon technology in violet and straw-tube technology in cyan. The Figure was obtained in [12](left). Track types visualisation depending on which track stations provided hits. For the study of  $B^+ \rightarrow \mu^+ \mu^- \mu^+ \nu$  decays only, **Long track**, are considered as muons will travel to the end of the detector leaving the hits all along. Figure is taken from [13] (right).

Most of the physics analyses use long tracks, tracks leaving hits in **VELO** and **T1**, **T2** and **T3**, as they give most precise momenta estimates. VELO tracks leave hits only in  $R$  and  $\Phi$  sensor, but not in any other tracking stations, meaning that they must have left **LHCb** acceptance or they come from particles produced backwards and hence are

useful for  $PV$  reconstruction. Upstream tracks are formed by tracks leaving hits in **VELO** and TT only. These are usually low momentum particles, which are bent out **LHCb** acceptance while traversing the magnet. Long-lived particles such as  $\Lambda$  or  $K_s^0$  will only decay outside of the **VELO** acceptance and hence will produce no hits until TT and T1, T2 and T3 forming downstream tracks. T-track is track type that only have hits in T1, T2 and T3. Again this could be due to presence of long-lived particles or due to secondary interactions in the detector.

In general, the track reconstruction software starts with *pattern recognition*, where several hits in one part of a tracking subdetector are identified and form *track seeds*, which are then extrapolated and combined with hits in other tracking subdetector provided this subdetector sits in low magnetic field. The long track candidates are formed and fitted with a Kalman filter [14], where because of the material present in the detector, corrections for energy losses as well as multiple scattering are incorporated.

Sometimes *pattern recognition* may combine random hits into a track, *ghost track*, or several tracks could be made out of same hits, *clone track*. Presence of these tracks are heavily suppressed with different techniques - such as establishing ghost probability - variable based on the output of neural network combining track  $\chi^2$  and missing hits in the subdetectors.

Mass uncertainty is one of the crucial parameters to minimize as it provides opportunity for high precision measurements by better separations from backgrounds. It strongly correlates with momentum resolution that is obtained using tracking. Resulting relative momentum uncertainty (0.5-1.1%) on long tracks using  $J/\psi \rightarrow \mu^+ \mu^-$  using *tag and probe* can be seen in Figure 2.8. It varies logarithmically with increasing momentum.

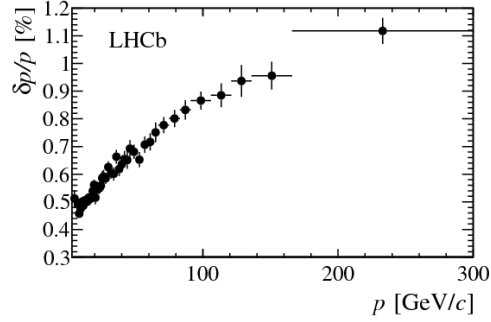


Figure 2.8: Momentum resolution of long tracks measured using "tag and probe" method at LHCb. The decay channel  $J/\psi^+ \rightarrow \mu^+ \mu^-$  is analyzed.

## 2.4 Ring Imaging Detectors

Particle identification, **PID**, at **LHCb** relies heavily on two dedicated Ring Imaging subdetectors. These detectors take advantage of the phenomena, emission of Cerenkov light, which happens when a charged particle travels through a medium at a speed faster than the phase velocity of light in that medium. This cone of light is emitted at an angle  $\theta$  with respect to the charged particle's trajectory. Using the knowledge of refractive index of the medium,  $n$ , and momentum  $p$  that is measured using tracking, mass  $m$  of the particle can be obtained through:

$$\cos \theta_c = \frac{\sqrt{m^2 + p^2}}{pn}. \quad (2.2)$$

As the momentum and mass are intrinsic properties of passing particle, the momentum identification range is limited by the choice of medium, also known as radiator. For very low-momentum particle, as  $\cos \theta_c \rightarrow 1$ , the particle is not producing any Cerenkov light cone. At the very high momentum, as  $\cos \theta_c \rightarrow 0$ , there is saturation point as all species of particles will emit the light at the same Cherenkov angle, hence all the

discriminating power will be lost.

Low momentum (2-60 GeV) particles are identified in the upstream RICH1 detector and high momentum particles (15-100) GeV are analyzed downstream in RICH2. RICH1 covers  $\pm 25$ -300 mrad in x-z plane,  $\pm 250$  mrad in the x-y plane, using either gaseous Aerogel ( $n = 1.03$ ) and  $C_4F_{10}$  ( $n = 1.0014$ ) as radiators. RICH2 has more limited acceptance of  $\pm 15$ -120 mrad in x-y plane and  $\pm 100$  mrad in x-z plane and uses  $CF_4$  as radiator, with lower  $n = 1.0005$ . The discrimination power between different particles can be seen [Figure 2.9](#).

Both RICH1 and RICH2 use set of spherical primary mirrors to guide the photons onto the flat secondary mirrors which are then further focused into Cerenkov rings onto the surface of Hybrid Photon Multipliers, [HPD](#). The schmematic view of a particle passing through RICH1 can be also seen in [Figure 2.9](#).

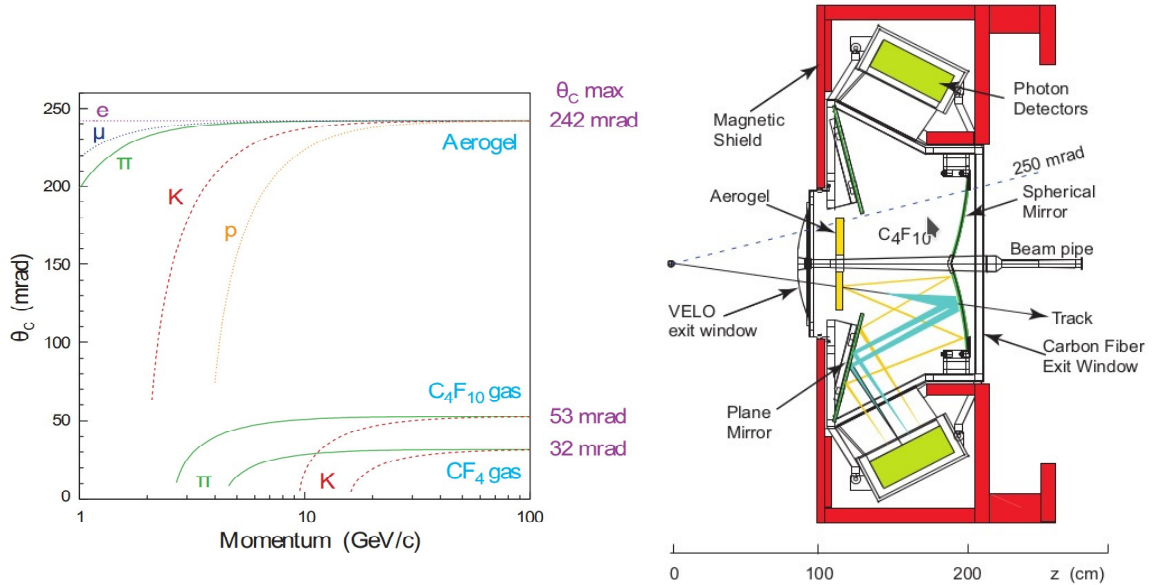


Figure 2.9: Separation power for different species of particles in momentum-Cerenkov angle plane (left). Schematic diagram of RICH1 layout (right). Boths figures are taken from [\[10\]](#).

## 2.5 RICH Reconstruction and Performance

In order to establish species of particles for each track, the Cerenkov angle is combined with the track momentum measured by tracking. In practice, however, as **RICH** detectors operate in high track density environment, many Cerenkov rings will be overlapping and hence a complex pattern recognition algorithm is deployed [15].

For each event, the **RICH** computes full event likelihood that is consistent with assigning pion mass hypothesis for all tracks given the observed hit distribution read out by **HPD**. The algorithm then iterates through all other possible particle species, ( $e, \mu, \pi, K$ , proton, deuteron), assigning new full event likelihood for a given track, having all other hypotheses fixed. The mass hypothesis with the highest full event likelihood is assigned to the track and this process is repeated for all the tracks in the event, until no improvement is found.

Results of this algorithm provide likelihood variables,  $DLL_x$ , that quantify the strenght of the chosen species hypothesis against pion hypothesis,

$$DLL_x = \log(\mathcal{L})_x - \log(\mathcal{L})_\pi \quad x \in e, \mu, K, \text{proton}, \text{deuteron}. \quad (2.3)$$

By calculating  $DLL_{x_1} - DLL_{x_2}$ , one can obtain discriminative strenght between any two species.

### 2.5.1 RICH performance

In order to measure the performance of the **PID** computed by **RICH**, populous calibration samples with very little background contamination are required. In order not to bias results, these samples have no **PID** constraints themselves and are reconstructed solely using kinematic information. For studies of pion/kaon efficiencies,  $D^{*+} \rightarrow D^0(K^-\pi^+)\pi^+$  background-subtracted samples are used, whereby the daughter tracks of  $D^0$  become proxies for evaluation. The probability of correctly identifying kaon given certain constraint on  $DLL_K$ , identification efficiency (**ID**), and probability of mistakenly swapping pion identification, **MisID** efficiency, are summarized in

Figure 2.10. Identification probabilities of  $\approx 85\%$  with misidentification rate of  $\approx 3\%$  provide invaluable discriminating separation between kaon and pion.

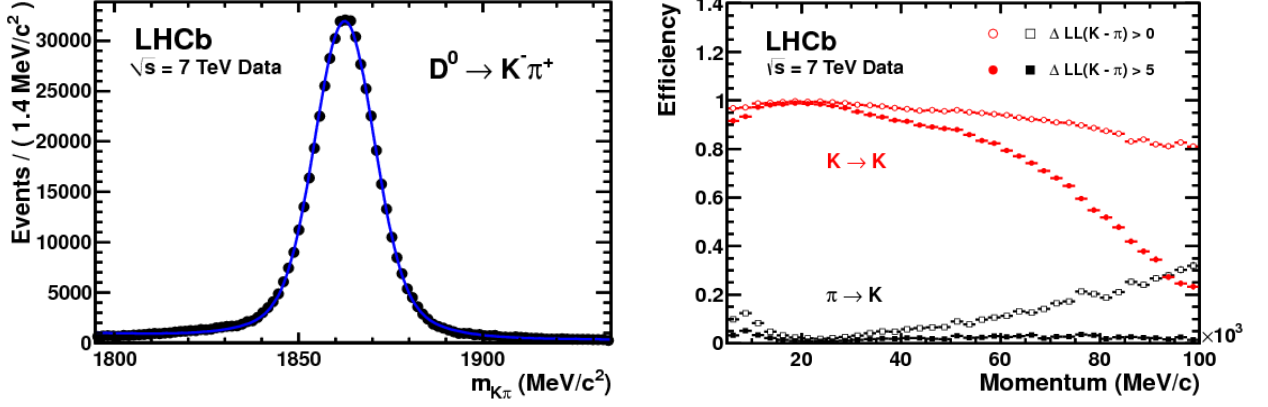


Figure 2.10: Invariant mass distribution of  $D^0$  data sample (in black) overlaid with fit to both background and signal (in blue) (left). An example of kaon ID (red) and MisID (black) efficiency as a function of momentum under two PID hypotheses,  $DLL_K > 0$  (empty) and  $DLL_K > 5$  (filled) (right). Both figures are taken from [16].

In search for  $B^0$  and  $B_s^0$  decaying to  $h^+ h^-$ , where  $h \in K, \pi$ ,  $\pi^+ \pi^-$  invariant mass spectra with and without PID  $DLL_x$  requirements can be seen in Figure 2.11. These plots clearly demonstrate increase in sensitivity searching for  $B^0 \rightarrow \pi^+ \pi^-$  signal amongst other components.



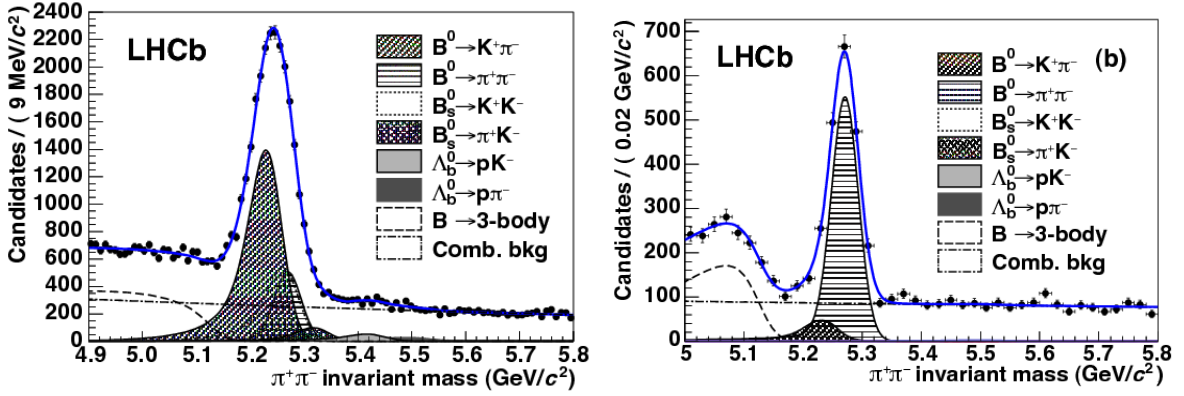


Figure 2.11:  $\pi^+\pi^-$  invariant mass distributions obtained using kinematic constraints only (left) and also using PID constraints (right) in order to isolate  $B^0 \rightarrow \pi^+\pi^-$  peak. This figure is taken from [17].

## 2.6 Calorimetry

As many other particle physics detectors, **LHCb** is equipped with series of subdetectors providing separation and **PID** tool for electrons, pions and photons. This separation is achieved because different particles interact at different distances, producing differently shaped showers of light. This part of detector is not only integral to the way **LHCb** trigger system works but it also provides precise measurement of energies of these objects. All the subcomponents discussed here operate on the same principle. The light from the scintillating material is guided to photomultiplier tubes by wavelength shifting fibres.

Electrons, pions and photons firstly encounter two planes of scintillating tiles: Scintillating Pad Detector (**SPD**), Preshower Detector (**PRS**) intersected by a wall of lead. The **SPD** senses the passage of charged particles whereas neutral particles will not be affected, distinguishing electrons from photons. The wall of lead initiates the electromagnetic shower, where photons are converted into electron-positron pairs, depositing sizable energy in the **PRS** allowing electron/pion separation.

The following Electromagnetic Calorimeter (**ECAL**) is based on sampling shashlik-

type technology, where scintillating tiles are alternated by lead plates measuring the energy deposit of electromagnetic showers. As the best energy resolution requires full energy deposit of energetic photons along the **ECAL**, the thickness is equivalent to 25 radiation lengths. The resulting resolution of **ECAL** is  $\frac{\sigma_E}{E} = \frac{10\%}{\sqrt{E}} \oplus 1\%$ , where  $E$  is in GeV.

On the other hand, **HCAL** sandwiches iron instead of lead as the absorber with thickness of 5.6 interaction length only, achieving resolution of  $\frac{\sigma_E}{E} = \frac{70\%}{\sqrt{E}} \oplus 10\%$  in beam tests. This poorer resolution however fulfills the requirements necessary for the main purpose of this detector, hadron trigger. Away from beampipe the granularity of cells is coarser to mirror the track occupancy as seen in Figure 2.12.

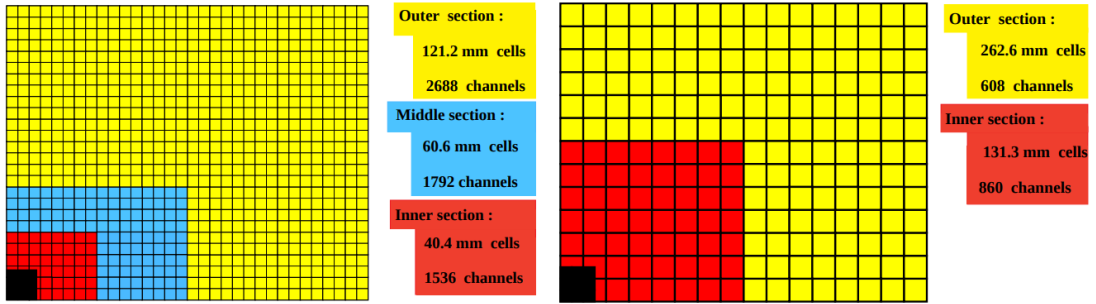


Figure 2.12: Granularity of **ECAL** (left) and **HCAL** (right) detectors. The figure was taken from [10].

## 2.7 Muon Stations

Muons are considered to be of fundamental importance to many flagship analyses by **LHCb**, such as the search for the rare  $B_s^0 \rightarrow \mu^+ \mu^-$  decay. Analysis of  $B^+ \rightarrow \mu^+ \mu^- \mu^+ \nu$  ofcourse relies heavily on good performance of this part of detector. Muon stations are positioned at the end of the detector, taking advantage of the low probability of interaction of muon previously in the detector.

**LHCb**'s five rectangular muon stations **M1-5** are positioned before and after calorime-

try system, with first station M1 upstream of the **SPD**, and four stations (M2-M5) downstream of **HCAL** as shown in Figure 2.13. The M1 station consists of 12 sets of three gas electron multiplier foils (triple-GEMs) in the region closest to the beam pipe, resisting the highest dose of radiation due to the highest particle flux. Its main use lies in improving the  $p_T$  resolution by  $\approx 10\%$ . M2-M5 station each consist of 276 multi-wire proportional chambers (**MWPCs**) filled with Ar – CO<sub>2</sub> – CF<sub>4</sub> gas mixture. They are interlayed with 0.8m iron walls, to provide stopping target to all particles, other than muons with momentum higher than 6 GeV/c. In order to ease the accessibility, like in **VELO**, all the stations are split into two independent mechanical sides, also known A and C side.

Each station is then further segmented into four increasingly larger regions away from the beam, R1 to R4. All the regions were constructed to cover the same acceptance, keeping the track occupancy constant accross the station. The granularity of the readout is higher in the horizontal plane to take advantage of magnet's horizontal bending plane.

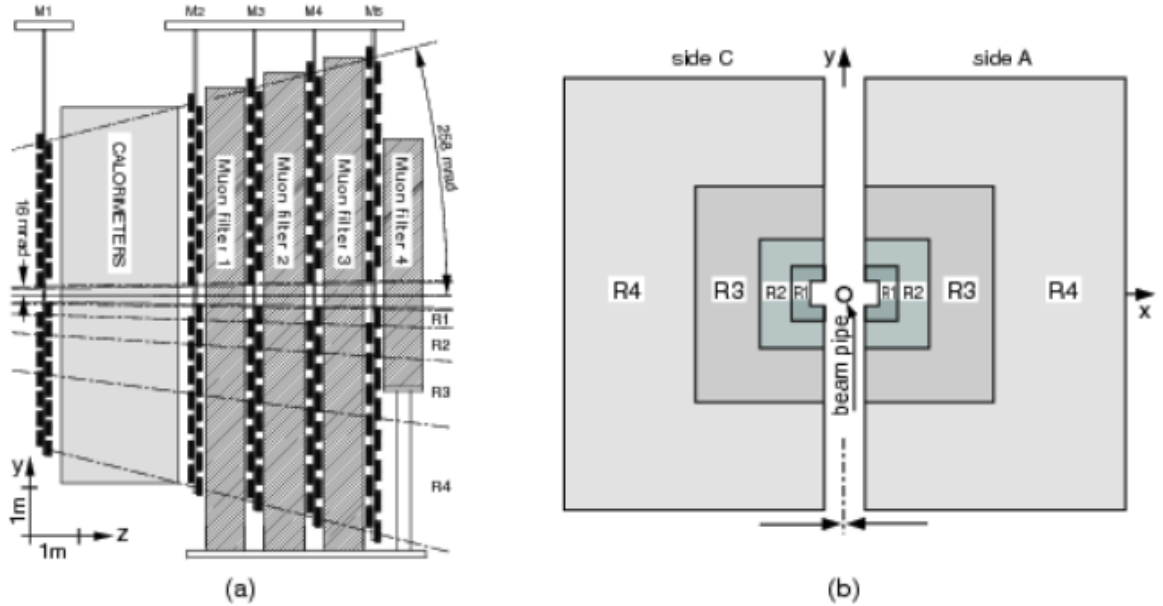


Figure 2.13: (a) Layout of the muon detector x-z plane and (b) x-y plane. This figure is taken from [18].

Both GEM and MWPCs operate on a same principle. In each station, position in the  $x - y$  plane is determined by ionizing electrons that come from muons passing through the detector, which are then attracted either to the closest anode mesh or wire mesh. The trigger is fired if the corresponding rectangular region in each station enregistered positive binary decision. This means the efficiency of each station must be  $\geq 99\%$  to give overall 95% trigger efficiency. Geometrical layout covers  $\approx 20\%$  muons originating in semileptonic  $b$  decays.

### 2.7.1 Muon Identification

Apart from triggering events with high enough  $p_T$  muons, muon stations provide necessary PID information for muon analyses. Offline variables mostly used for muon ID by analysts are

- **IsMuon**: Boolean decision of muon candidates with momentum-dependent categorisation. Long tracks with  $p > 3 \text{ GeV}/c$  are extrapolated to muon stations yielding  $x - y$  coordinates in  $M2 - M5$ , considering only tracks within acceptance. For each station, search for the hit information within elliptical area defined by momentum, field of interest (FOI), is performed. The hit requirements are summarized in Table 2.2.
- **muDLL**: Difference in log likelihoods computed using muon and non-muon hypothesis. These hypotheses are based on the proximity/distance  $D^2$  of the track extrapolation into the muon stations and corresponding closest sensed hits in those stations. Muon-like particle will tend to have sharper distribution in  $D^2$  as compared to other species. Protons were chosen for the calibration purposes giving broader distribution originating from punch-through protons, protons having coincident hit position to true muon, and random hits.
- **DLLmu**: For each track global likelihood is produced, by combination of muon and non-muon likelihood from **muDLL**, with the RICH different mass hypothesis

likelihoods, and calorimetry likelihood exploiting the energy deposits information. Like in **RICH** likelihoods, the default hypothesis corresponds to separation between muon and pion hypothesis.

Particle Momentum $p$	Hits in Muon Stations
$3 \text{ GeV}/c < p < 6 \text{ GeV}/c$	M1 & M2
$6 \text{ GeV}/c < p < 10 \text{ GeV}/c$	M1 & M2 & (M3    M4)
$10 \text{ GeV}/c < p$	M1, M2, M3 and M4

Table 2.2: Momentum-dependent definition IsMuon variable.

### 2.7.2 Muon Performance

As in hadron performance measurements, muon ID is determined using high statistics decay channel  $J/\psi \rightarrow \mu^+ \mu^-$  using tag-and-probe method. Mis-ID rates are computed using the same decay channels as previously. The summary of IsMuon **ID** and misid rates are presented in [Figure 2.14](#). Very high ID rate (above 90%) for relatively low misid probability (below 10%) performs the least well in low  $p_T$  bins as here the muons end up outside of the acceptance. The misid rates for kaon and pions are significantly higher in low momenta region as the dominant process causing this are prompt muons from decay-in-flight.

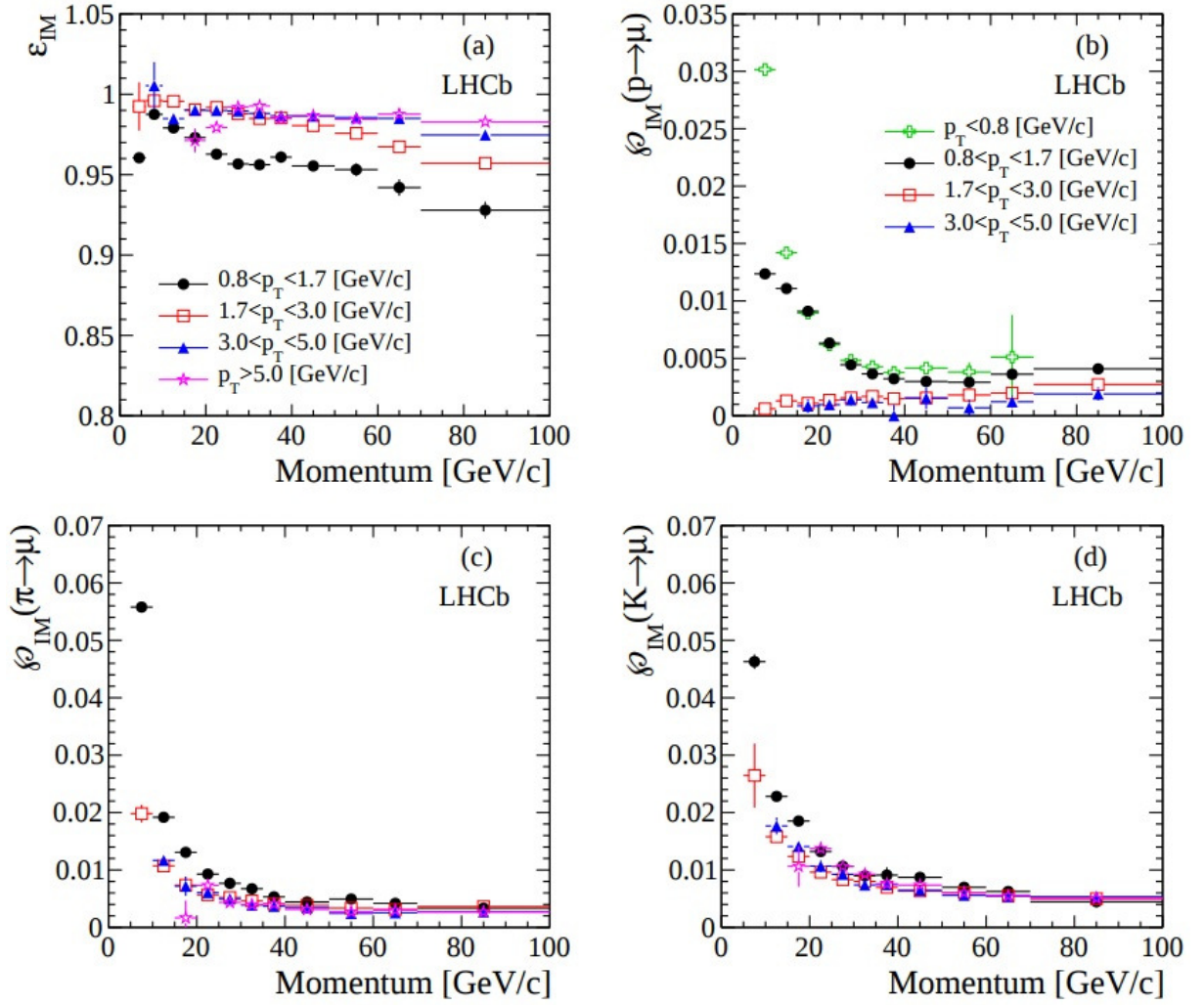


Figure 2.14: (a) Probability of correctly identifying muons as a function of momentum  $p$  in the bins of  $p_T$  for  $J/\psi \rightarrow \mu^+ \mu^-$  with IsMuon constraint. (c) Probability of incorrectly identifying pion (b) proton and (d) kaon as muon with IsMuon. This figure is taken from [19].

## 2.8 Trigger

Nowadays, big-data physics experiments have to make decisions on what kind of data they want to keep. The choice of interesting events is performed by series of decisions, which is cumulatively known as trigger. LHCb trigger system was build

around constraints posed by the run conditions, read-out capabilities and available disk space. In Run I and Run II LHCb has at its disposal the multistage trigger consisting of hardware-based level 0 trigger (**L0**) and software-based high level trigger (**HLT**).

**L0** reduces the rate of data from 40 MHz to 1 MHz by employing five trigger decisions, also known as lines. First three lines make decision using calorimeter information about the transverse energy,  $E_T$ , whether it is photon, electron or hadron causing the shower energy deposit. Two other lines are reading out information from the muon system by looking for transverse momentum,  $p_T$ , of muon and dimuon (two muon tracks) objects. Efficiencies of L0 muon triggers are evaluated using  $B^+ \rightarrow (J/\psi \rightarrow \mu^+ \mu^-) K^+$  decays. Hadron trigger efficiency in different decay channels can be seen in Figure 2.15.

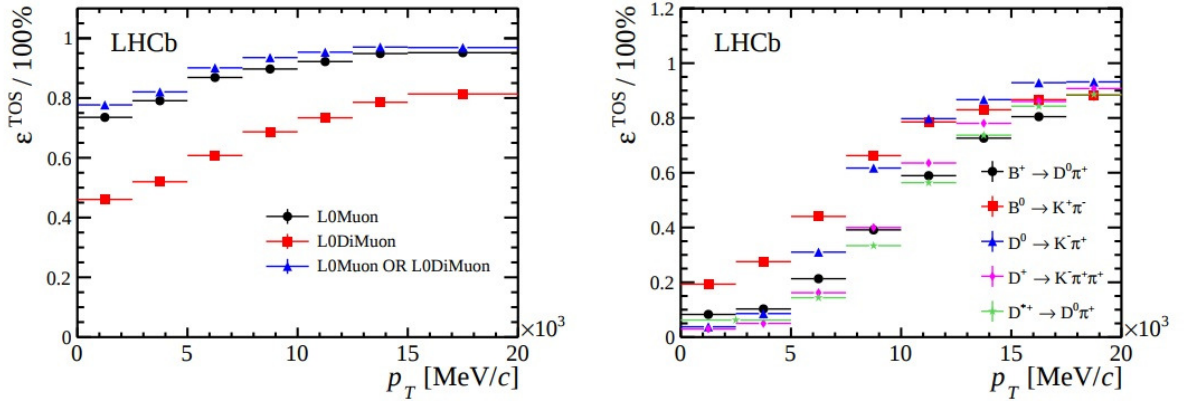


Figure 2.15: **TOS** efficiency as a function of  $p_T$  for muon-based decisions (left). **TOS** efficiency for different decays using L0 hadron trigger lines. This figure is taken from [18].

Software-based **HLT** then further reduces the rate from 1 MHz down to 40 – 80 kHz which can be safely stored to disk. The first stage of the **HLT**, (**HLT1**), performs limited track reconstruction and hence makes decision based on the presence of charged tracks in the event. **HLT1** uses **VELO** hits to reconstructs **PVs** and **VELO** tracks by using 3D pattern recognition. As **LHCb**'s primary mission is to study decays of hadrons containing  $b$  and  $c$  quark, **HLT1** will make decision based on the track segments being



displaced (having high **IP**) with respect to the **PV**. For events selected by the *L0Muon*, an attempt is made to match the **VELO** tracks to hits observed in the vertical plane in the muon chambers due to magnet bending plane. By computing the track  $\chi^2$ , the potential muon track candidates are selected. Finally, the **VELO** tracks and muon tracks are extrapolated into the **OT** or **IT** trackers, allowing for so called *forward tracking*, whereby  $p$  and  $p_T$  requirements are imposed to reduce processing time. Each track is then fitted with fast Kalman filter providing the  $\chi^2$  of the fit. The corresponding performance of **HLT1** trigger lines are shown in Figure 2.16.

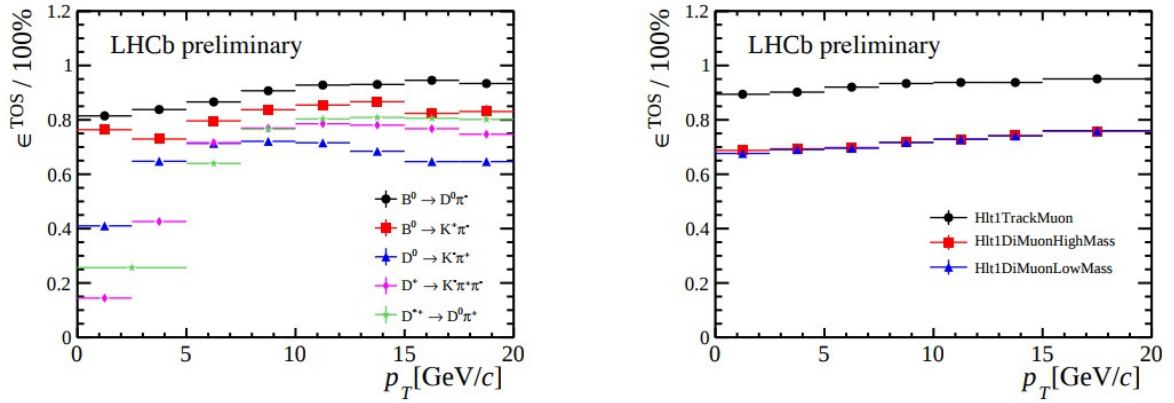


Figure 2.16: **HLT1** efficiencies of the corresponding triggers using the same proxy as in Figure 2.15. This figure is taken from [20].

The second stage **HLT2** reduces the rate to 5 kHz that can be safely written to disk. **HLT2** consists of a series of decisions based on a full reconstruction of either groups of decays or specific decay modes. *Topological triggers* exploit the vertex and track information (topology) of  $b$ -hadron decays. By employing multivariate techniques 2,3 or 4-body decays away from **PV** are reconstructed. To account for decays where final state particle is not fully reconstructed, corrected mass serves as an input variable in the the **BDT**. Dedicated lines are also written to reconstruct muon and dimuon channels allowing for both prompt  $J/\psi$  and  $B \rightarrow J/\psi X$  studies. Finally *Exclusive triggers* concentrating on selecting events with  $c\bar{c}$  do selection very similar to the offline selection but without



**PID** cuts and with *prescales*, only allowed in a certain fraction of events, is applied.

In the end, selected events have their trigger decisions categorized by different type. An event where signal candidate caused the trigger to fire is known to be Trigger on Signal (**TOS**). An event where it is non-signal like particle causing the trigger decision to occur, Trigger Independent of Signal (**TIS**) is used. Finally, if only by combination of signal particle together with other particle's properties in the event produce affirmative decision, then these events are categorized as **TIS & TOS = TISTOS**.

Between the Run I and Run II period there has been a change in how the software trigger operates, which can be seen in [Figure 2.17](#). As more timing budget was introduced for both **HLT1** and **HLT2**, **LHCb** took advantage in upgrading the trigger system. By introducing update of calibration and alignment constants of the relevant subdetectors before the data is sent to permanent disk, *online reconstruction*, defined as being produced at trigger farm, is the same as the *offline reconstruction*, defined as reconstruction made when data reached the permanent disk. Hence, there is enhancement of available information, such as the **PID** in the **HLT**, which can be then used at the trigger level. (Mention Turbo?).

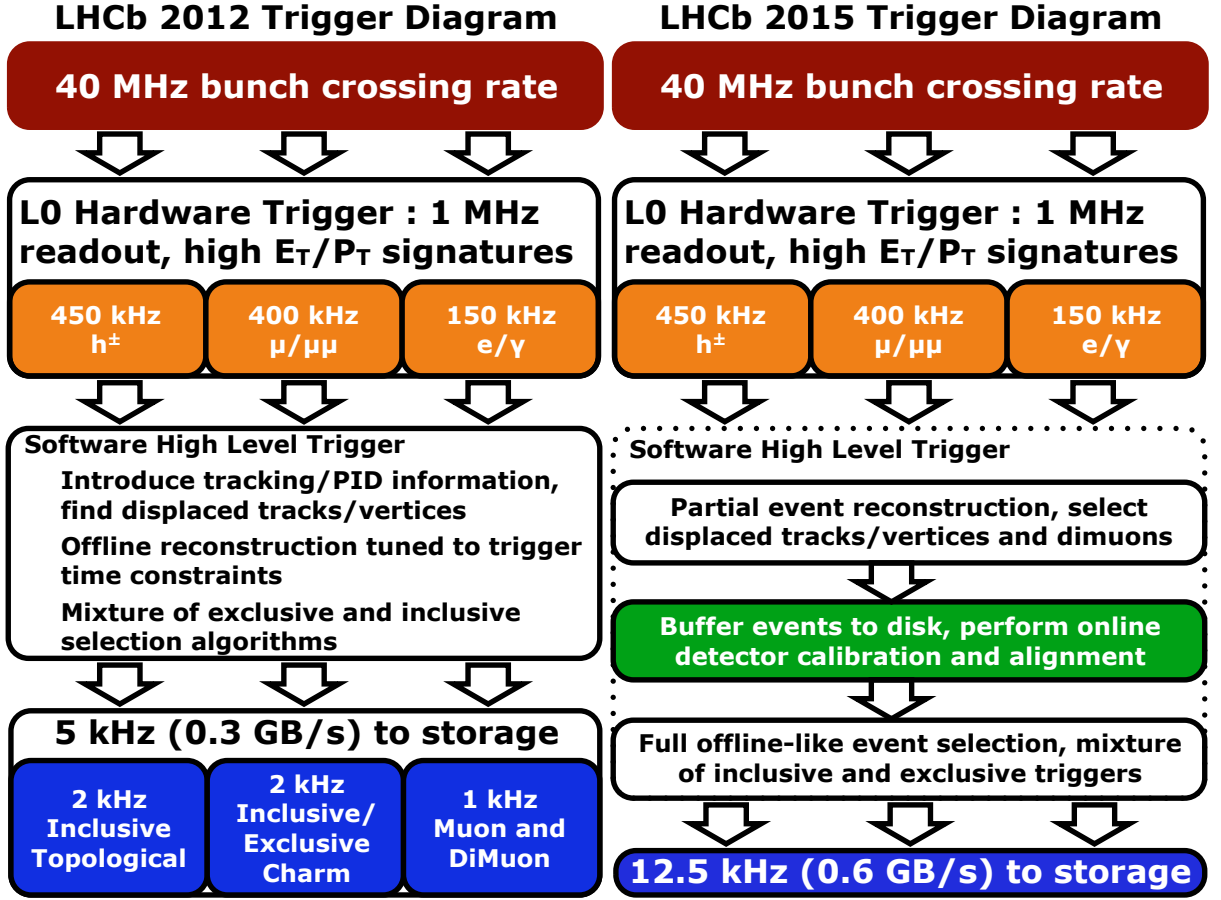


Figure 2.17: Trigger scheme differences between Run I and Run II. Figures obtained from [21]

## 2.9 Simulation

In order to optimise the event selections, extract efficiencies and model the backgrounds, a full Monte Carlo Simulation **MC** starting from simulation the  $pp$  collision to detector readout of decay of interest is produced. The  $pp$  collisions within **LHCb** configuration [22] are simulated with Pythia 6.4 [23] and Pythia 8.2 [2]. **LHCb** specific settings are mostly related to running conditions: luminosity, number of collisions per bunch crossing as well as contamination from other bunches, *spill-over*.

In the  $pp$  collision, the  $b$  and  $c$  production mechanisms are simulated and then the following  $b\bar{b}$  or  $c\bar{c}$  pair is hadronized into hadrons of interest. In this thesis and the

analysis presented,  $B^+$  is the hadron of interest. Hadrons are then further decayed using EVTGEN [24] into the chosen decay products. In this stage, different physics models or inputs from theory can be configured. At the same time some initial CPU-friendly selection is established, usually requiring the hadrons to be contained within the forward detector's acceptance. In order to account for the effects of QED radiative corrections, PHOTOS [25] algorithm can be used. All of this combined establishes *generator-level simulation* of LHCb.

In the next phase, *detector simulation*, the interactions of the all the particles with the detector, transport, as well as detector's response are simulated using the C++ GEANT4 toolkit [26], [27]. LHCb's interface to GEANT4 is detailed in [28].

### 2.9.1 Differences in Simulation And Data

Despite the complexity and best intention of the LHCb simulation, there are several shortcomings that require correction treatment. The most affected variables necessary for physics analyses that one needs to consider are IP resolution, track reconstruction efficiencies, PID variables and track occupancy.

The IP resolution shows better trend in the simulation then in the data due to the mismodelling of material description of VELO simulation. As shown in Figure 2.18 IP resolution does greatly differ depending the variation of material density of VELO. Around  $\phi = \pm\pi/2$ , where the two VELO parts overlap, the material difference causes the discrepancy. It can be corrected either by reweighting to data or by smearing the resolution wit Gaussian distribution.

Track reconstruction efficiency is also not reproduced very well in certain kinematical bins, again due to modelling of scattering interactions.

The most critical problem that needs to be addressed in the presented analysis are the inaccuracies of PID variables, which are mismodelled in the simulation. The origin of this problem arises as a consequence of much lower estimate of low momentum tracks in the detector making the photoelectron background underestimated. This

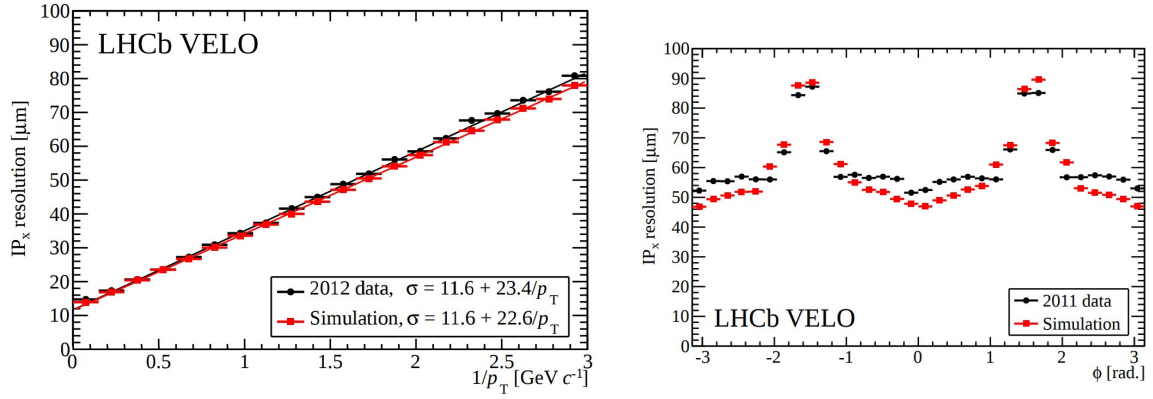


Figure 2.18: IP resolution in x-direction comparing the data and simulation output for 2012 data-taking period (left). IP resolution in x-direction comparing the data and simulation output for 2011 data-taking period as a function of angle,  $\phi$  (right). These figures are taken from [11].

results in better performance of separation power in simulation and is corrected using real data calibration.

# Chapter 3

## Discovering (Setting Limit for)

### $B^+ \rightarrow \mu^+ \mu^- \mu^+ \nu$ at LHCb

*LHCb's flagship analyses contain several muons in the final state coming from differently flavoured B mesons. Despite being in this category, search for  $B^+ \rightarrow \mu^+ \mu^- \mu^+ \nu$  is limited by the rareness of its occurrence as well as different backgrounds that can mimic its signature in the detector. Moreover, presence of invisible neutrino does induce uncertainties into reconstruction. This [chapter 3](#) will concentrate on characterisation of backgrounds as well as selection that is performed in order to reduce the backgrounds.*

#### 3.1 Topology of $B^+ \rightarrow \mu^+ \mu^- \mu^+ \nu$ at LHCb

Upon hadronisation of  $b\bar{b}$  pair  $B^\pm$  particle will travel less than a millimetre in the laboratory frame of reference before it decays into its decay products. This allows reconstruction of a primary vertex **PV** and its decay vertex, *secondary vertex* **SV**. By joining these vertices, direction as well as length of the  $B^\pm$  existence, also known as flight distance (**FD**), can be established. In order to infer information about kinematic properties of  $B^\pm$ , the decay products are studied. All three muons are used to reconstruct the visible four-momentum. By conservation of momentum with respects to the direction of the flight of  $B^\pm$ , neutrino is assigned all missing momentum transverse to

the direction of the flight of  $B^\pm$ . The schematic diagram can be seen in Figure 3.1.

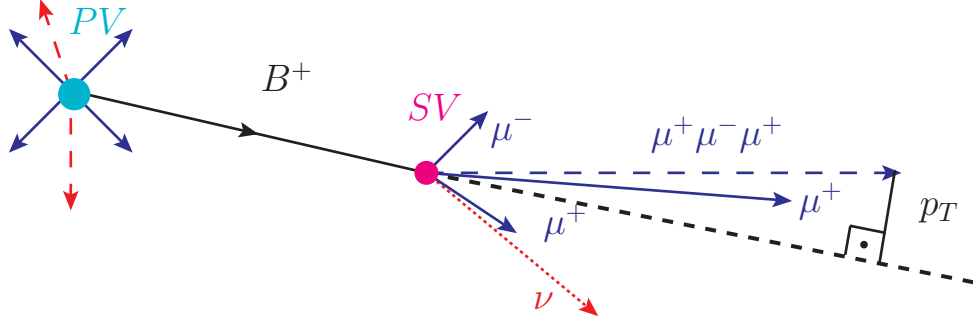


Figure 3.1: Schematic view of  $B^+ \rightarrow \mu^+ \mu^- \mu^+ \nu$  decay. At  $pp$  interaction point, or  $PV$ ,  $b\bar{b}$  pair hadronizes into  $B^\pm$ .  $B^\pm$  flies some distance before decaying into three muons and neutrino. All charged tracks (in filled-blue) seen can be combined into four-vector representing the visible part of the decay (semifilled-blue). Information about invisible neutrino (semifilled-red) are deduced from the conservation of momentum with respect to the direction of the flight of  $B^\pm$ . Neglecting momentum component parallel to the direction of flight for neutrino, transverse component of momentum is given.

Altogether it allows for reconstruction of a quantity, *corrected mass*, that plays similar role to invariant mass in fully reconstructed decays. Invariant mass is ususally used in LHCb for fitting distribution from which physics results are extracted as it distinguishes well signal from background and there is minimal modelling problem.

*Corrected mass* is defined as

$$M_{corr} = \sqrt{M^2 + |p_T^2| + |p_T|}, \quad (3.1)$$

where the  $M^2$  is the invariant visible mass squared and  $p_T^2$  is the missing momentum squared transverse to the direction of  $B^+$  flight.

$M_{corr}$  can be thought of as the the minimal correction to the visible mass to account for the missing neutrino information. The resolution on the *corrected mass* hence becomes a critical quantity that needs to be understood. As the method of reconstruction of corrected mass relies heavily on the knowledge of  $B^\pm$  flight direction, the resolution of

**PV** position and **SV** vertex is crucial. Let  $\vec{x}_{PV} = \{x_{PV}, y_{PV}, z_{PV}\}$ ,  $\vec{x}_{SV} = \{x_{SV}, y_{SV}, z_{SV}\}$  be **PV** and **SV** vertex position and  $\vec{p} = \{E, p_x, p_y, p_z\}$  be the visible trimuon four-momentum. Then the missing transverse momentum to the direction of the flight  $p_T$  (momentum of the neutrino) is

$$p_T^2 = |\vec{p} - (\vec{x}_{SV} - \vec{x}_{PV}) \frac{\vec{p} \cdot (\vec{x}_{SV} - \vec{x}_{PV})}{|\vec{x}_{SV} - \vec{x}_{PV}|^2}|^2 \quad (3.2)$$

In general in order to propagate error on  $f(x, y, z)$ , where  $x, y, z$  are independent variables, the variance of  $f(x, y, z)$

$$\langle f^2 - \langle f \rangle^2 \rangle = \langle f(x + \delta x, y + \delta y, z + \delta z)^2 - f(\langle x \rangle, \langle y \rangle, \langle z \rangle)^2 \rangle \quad (3.3)$$

Using first order Taylor expansion of variance and rewriting into the matrix form:

$$\begin{bmatrix} \frac{\partial f}{\partial x} & \frac{\partial f}{\partial y} & \frac{\partial f}{\partial z} \end{bmatrix} \begin{bmatrix} \delta x^2 & \delta x \delta y & \delta x \delta z \\ \delta y \delta x & \delta y^2 & \delta y \delta z \\ \delta z \delta x & \delta z \delta y & \delta z^2 \end{bmatrix} \begin{bmatrix} \frac{\partial f}{\partial x} \\ \frac{\partial f}{\partial y} \\ \frac{\partial f}{\partial z} \end{bmatrix} \quad (3.4)$$

So now assuming that  $x = \vec{x}_{PV}$ ,  $y = \vec{x}_{SV}$  and  $z = \vec{p}$ ,

$$\nabla_{x_{PV}}^T \text{COV}_{x_{PV}} \nabla_{x_{PV}} + \nabla_{x_{SV}}^T \text{COV}_{x_{SV}} \nabla_{x_{SV}} + \nabla_p^T \text{COV}_p \nabla_p \quad (3.5)$$

where COV is the covariance matrix.

In conclusion in order to calculate error on *corrected mass*,  $\delta_{corr m}$

$$\delta_{corr m} = \sqrt{\langle f^2 - \langle f \rangle^2 \rangle} = \sqrt{\nabla_{x_{PV}}^T \text{COV}_{x_{PV}} \nabla_{x_{PV}} + \nabla_{x_{SV}}^T \text{COV}_{x_{SV}} \nabla_{x_{SV}} + \nabla_p^T \text{COV}_p \nabla_p} \quad (3.6)$$

which can be calculated analytically (method used for all the plots) or using numerical approximation of first derivative of *finite diffences*.

## 3.2 Sources of Backgrounds

The largest background that can be will be looking similar to signal comes from so called *cascade decays*, where  $b \rightarrow c \rightarrow s$  or  $(\bar{b} \rightarrow \bar{c} \rightarrow \bar{s})$  transition occurs. A typical example of this background in hadronic terms is  $B^+ \rightarrow (\bar{D}^0 \rightarrow (K^+ \rightarrow \mu^- \nu) \mu^+ \nu)$ , where  $K^+$  is misidentified as muon. Because  $K^+$  is misidentified as muon, this type of background is denoted as misID background. In fact, any misidentified particle species belongs to the misID background category. If the sign of the misidentified particle agrees with the sign of the mother  $B^\pm$ , it belongs to the same sign misID background (*SS misID*) background. In the event where opposite sign particle is misidentified, (*OS misID*) is used. However, *OS misID* background is expected to have smaller rate as the misidentified particle would have to proceed via decays with additional particles or if coming as product from other  $b$  hadronization.



# Bibliography

- [1] *Image of the cern accelerator complex from* <https://cds.cern.ch/record/2225847>, Accessed in 2017.
- [2] T. Sjostrand, S. Mrenna, and P. Z. Skands, *A Brief Introduction to PYTHIA 8.1*, **Comput. Phys. Commun.** **178** (2008) 852, [arXiv:0710.3820](#).
- [3] LHCb collaboration, *Image of the acceptance of using simulation taken from* [https://lhcb.web.cern.ch/lhcb/speakersbureau/html/bb\\_productionangles.html](https://lhcb.web.cern.ch/lhcb/speakersbureau/html/bb_productionangles.html), Accessed in 2017.
- [4] G. Raven, *LHCb: Status and prospects*, **Nucl. Phys. Proc. Suppl.** **163** (2007) 153, [153(2007)].
- [5] LHCb collaboration, R. Aaij *et al.*, *Measurement of  $\sigma(pp \rightarrow b\bar{b}X)$  at  $\sqrt{s} = 7$  TeV in the forward region*, **Phys. Lett.** **B694** (2010) 209, [arXiv:1009.2731](#).
- [6] LHCb collaboration, R. Aaij *et al.*, *Measurement of the  $b$ -quark production cross-section in 7 and 13 TeV  $pp$  collisions*, **Phys. Rev. Lett.** **118** (2017) 052002, Erratum **ibid.** **119** (2017) 169901, [arXiv:1612.05140](#).
- [7] *Image of the lhcb detector from* <http://cds.cern.ch/record/1087860>, Accessed in 2017.
- [8] *Image of the luminosity overview from* <https://lbggroups.cern.ch/online/operationsplots>, Accessed in 2017.

- [9] LHCb collaboration, R. Aaij *et al.*, *LHCb detector performance*, *Int. J. Mod. Phys. A* **30** (2015) 1530022, [arXiv:1412.6352](#).
- [10] The LHCb collaboration, A. A. Alves, Jr. *et al.*, *The LHCb Detector at the LHC*, *JINST* **3** (2008) S08005.
- [11] R. Aaij *et al.*, *Performance of the LHCb Vertex Locator*, *JINST* **9** (2014) 09007, [arXiv:1405.7808](#).
- [12] *Image of the Tracker System taken from the LHCb public web page*, Accessed in 2017.
- [13] LHCb collaboration, R. Aaij *et al.*, *Measurement of the track reconstruction efficiency at LHCb*, *JINST* **10** (2015) P02007, [arXiv:1408.1251](#).
- [14] R. Hierk, M. Merk, M. Needham, and R. Van der Eijk, *Performance of the LHCb 00 track fitting software*, Tech. Rep. LHCb-2000-086, CERN, Geneva, Aug, 2000.
- [15] LHCb, R. Forty, *RICH pattern recognition for LHCb*, *Nucl. Instrum. Meth. A* **433** (1999) 257.
- [16] M. Adinolfi *et al.*, *Performance of the LHCb RICH detector at the LHC*, *Eur. Phys. J. C* **73** (2013) 2431, [arXiv:1211.6759](#).
- [17] LHCb collaboration, R. Aaij *et al.*, *Measurement of  $b$ -hadron branching fractions for two-body decays into charmless charged hadrons*, *JHEP* **10** (2012) 037, [arXiv:1206.2794](#).
- [18] A. A. Alves Jr. *et al.*, *Performance of the LHCb muon system*, *JINST* **8** (2013) P02022, [arXiv:1211.1346](#).
- [19] F. Archilli *et al.*, *Performance of the muon identification at LHCb*, *JINST* **8** (2013) P10020, [arXiv:1306.0249](#).
- [20] LHCb HLT project, J. Albrecht, V. V. Gligorov, G. Raven, and S. Tolk, *Performance of the LHCb High Level Trigger in 2012*, *J. Phys. Conf. Ser.* **513** (2014) 012001, [arXiv:1310.8544](#).

- [21] *Images of different trigger schemes taken from the LHCb speaker's bureau web page*, Accessed in 2018.
- [22] LHCb, I. Belyaev *et al.*, *Handling of the generation of primary events in Gauss, the LHCb simulation framework*, *J. Phys. Conf. Ser.* **331** (2011) 032047.
- [23] T. Sjostrand, S. Mrenna, and P. Z. Skands, *PYTHIA 6.4 Physics and Manual*, *JHEP* **05** (2006) 026, [arXiv:hep-ph/0603175](#).
- [24] D. J. Lange, *The EvtGen particle decay simulation package*, *Nucl. Instrum. Meth.* **A462** (2001) 152.
- [25] P. Golonka and Z. Was, *PHOTOS Monte Carlo: A Precision tool for QED corrections in Z and W decays*, *Eur. Phys. J.* **C45** (2006) 97, [arXiv:hep-ph/0506026](#).
- [26] Geant4 collaboration, J. Allison *et al.*, *Geant4 developments and applications*, *IEEE Trans. Nucl. Sci.* **53** (2006) 270.
- [27] Geant4 collaboration, S. Agostinelli *et al.*, *Geant4: a simulation toolkit*, *Nucl. Instrum. Meth.* **A506** (2003) 250.
- [28] LHCb, M. Clemencic *et al.*, *The LHCb simulation application, Gauss: Design, evolution and experience*, *J. Phys. Conf. Ser.* **331** (2011) 032023.

# Appendices

# Appendix A

## Boosted Decision Trees

Many rare decay analyses make extensive use of BDTs and they are important in the  $\Lambda_b^0 \rightarrow p\pi^-\mu^+\mu^-$  analysis. Firstly, the concept of a decision tree is introduced followed by a brief explanation of boosted decision trees.

A decision tree, in the context of data mining, is a supervised machine learning method which allows for the prediction of the value of a target variable based on several input variables. In particle physics, the purpose of the decision tree is to classify an event as being either signal or background, based on the event's input variables. The input variables,  $\{x_i\}$ , are various physics parameters. Each cut point in the tree is referred to as a node and the final nodes are referred to as leaves. A very simple example is shown in [Figure A.1](#). The purity,  $P$ , of a leaf refers to the fraction of the weight of a leaf due to signal events, e.g. if a leaf had 20 signal events and 15 background events it would have a purity of 0.75. If a leaf has a purity larger than 0.5 it is deemed to correspond to signal and if lower, to background.

A decision tree is constructed by a process called training. For this, samples of known signal and background events are used. These samples could be either simulation or data. For each  $x_i$  the best dividing point is decided, that is, the cut that gives the best separation between signal and background. This optimum point is decided by using the Gini index defined as

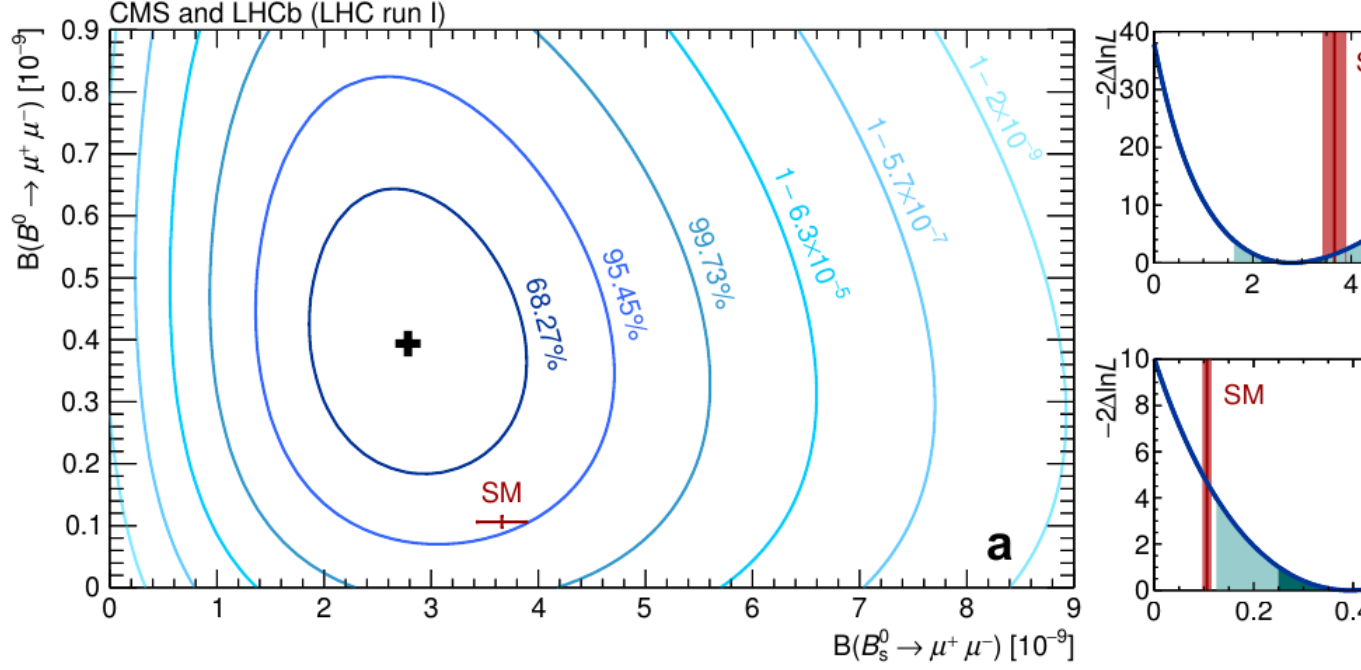


Figure A.1: An example decision tree. The S and B stand for ‘Signal-like’ and ‘Background-like’. The  $\beta_i$  variables refer to the cut values chosen by the machine learning algorithm after the tree has been trained on signal and background samples. The blue ovals represent final nodes called leafs, which each leaf having an associated purity, i.e. the fraction of the weight of a leaf due to signal events.

$$Gini = \sum_{i=1}^n W_i P(1 - P), \quad (\text{A.1})$$

where  $W_i$  is weight of the  $i^{th}$  event, which would generally be unity for the case of a non-boosted decision tree. The cutting point is then found by maximising the separation,  $\Delta$ , between the Gini index of the parent node and the combined Gini index of the child nodes, as given in [Equation A.2](#)

$$\Delta = Gini_{parent} - Gini_{child_1} - Gini_{child_2}. \quad (\text{A.2})$$

The depth of a tree (the maximum number of cuts or nodes) is normally a number

specified before the training begins.

Boosting a decision tree involves training many trees ( $\mathcal{O} \sim 1000$ ) and giving misclassified events a higher weight. A misclassified event is defined as a known signal event being placed on a background leaf and vice versa. By giving the events which are difficult to classify more weight, the next tree to be trained will effectively have to work harder in order to classify events correctly.

The total score on an event is deduced by following an event through from tree to tree and, for the algorithms used in this thesis, is simply given by the weighted sum of the scores over the individual trees.

Data sets are split into two (or more) sub samples, where one half is used for training the tree and the other is used for testing the tree, and the distributions of the event scores (the BDT output) for training and testing samples are compared for signal and background. Cases where the training sample performs better than the testing sample are referred to as over-trained trees, which is often due to the BDT becoming sensitive to the statistical fluctuations of the training sample.

The distribution of events scores for a given dataset can then be cut on in order to increase the fraction of signal events.

# Appendix B

## The *sPlot* technique

The *sPlot* technique is used extensively throughout this thesis. It is used in cases when there is a merged dataset which consists of data from different sources of data species, namely background and signal. These datasets are assumed to have two different sets of variables associated with the events they contain. Discriminating variables are those whose distributions are known for background and signal. Control variables are those whose distributions are unknown, or are assumed to be unknown.

The *sPlot* technique allows the distribution of the control variables for each data species to be deduced by using the species discriminating variable. This method relies on the assumption that there is no correlation between the discriminating variable and the control variable. The discriminating variable used in this thesis is always the mass distribution. The full mathematical description of the *sPlot* technique can be found in Ref [2], the key points are outlined here.

An unbinned extended maximum likelihood analysis of a data sample of several species is considered. The log-likelihood is expressed as

$$\mathcal{L} = \sum_{e=1}^N \left\{ \ln \sum_{i=1}^{N_s} N_i f_i(y_e) \right\} - \sum_{i=1}^{N_s} N_i, \quad (\text{B.1})$$

where  $N$  is the total number of events considered,  $N_s$  is the number of species of event (i.e. two - background and signal),  $N_i$  is the average number of expected events for



the  $i^{th}$  species,  $y$  represents the set of discriminating variables,  $f_i(y_e)$  is the value of the Probability Density Function (PDF) of  $y$  for event  $e$  for the  $i^{th}$  species and the control variable,  $x$ , does not appear in the expression of  $\mathcal{L}$  by definition.

For the simple (and not particularly practical) case of the control variable  $x$  being a function of  $y$ , i.e. completely correlated, one could naively assume that the probability of a given event of the discriminating variable  $y$  being of the species  $n$  would be given by

$$\mathcal{P}_n(y_e) = \frac{N_n f_n(y_e)}{\sum_{k=1}^{N_s} N_k f_k(y_e)}. \quad (\text{B.2})$$

The distribution for a control variable  $x$  for the  $n^{th}$  species,  $M_n(x)$ , can be deduced by histogramming in  $x$  and applying  $\mathcal{P}_n(y_e)$  as a weight to event  $e$ . In this scenario the probability,  $\mathcal{P}_n(y_e)$ , would run from 0 to 1.

In the case considered in this thesis, where  $x$  is entirely uncorrelated with  $y$ , it can be shown that  $\mathcal{P}_n(y_e)$  can be written as

$$\mathcal{P}_n(y_e) = \frac{\sum_{j=1}^{N_s} V_{nj} f_j(y_e)}{\sum_{k=1}^{N_s} N_k f_k(y_e)}, \quad (\text{B.3})$$

where  $V_{nj}$  is the covariance matrix between the species  $n$  and the  $j^{th}$  species. The inverse of this covariance matrix is given by the second derivative of  $-\mathcal{L}$  in [Equation B.1](#).

The quantity in [Equation B.3](#) is donated as the sWeight. In this thesis the species,  $n$ , in [Equation B.3](#) is always the signal. Because of the presence of the covariant derivative the sWeight of an event can be both positive and negative. The more negative an event is, the more likely it is to be background and vice versa for positive sWeights. The signal distribution for the control variable  $x$ ,  $M_s(x)$ , can again be deduced by histogramming events in  $x$ , applying the sWeight to each event.